SPE 122611

Non-Darcy Porous Media Flow According to the Barree and Conway Model: Laboratory and Numerical Modeling Studies

Bitao Lai, Jennifer L. Miskimins, and Yu-Shu Wu, Colorado School of Mines

This paper was prepared for presentation at the 2009 SPE Rocky Mountain Petroleum Technology Conference held in Denver, Colorado, USA, 14–16 April 2009.

Abstract
This paper presents supplementary laboratory data to show that a non-Darcy flow model, proposed by Barree and Conway in 2004, is capable of overcoming the limitation with the Forchheimer non-Darcy equation in high flow rates while describing the entire range of relationships between rate and potential gradient from low- to high-flow rates through proppant packs using a single equation or model. To supplement these laboratory findings, a numerical model is developed that incorporates the Barree and Conway model into a general-purpose reservoir simulator for modeling single-phase non-Darcy flow in porous and fractured media. In the numerical approach, flow through fractured rock is handled using a general multi-continuum approach, applicable to both continuum and discrete fracture conceptual models. The numerical formulation is based on a discretization using an unstructured grid of regular or irregular meshes, followed by time discretization carried out with a backward, first-order, finite-difference method. The final discrete nonlinear equations are handled fully implicitly, using Newton iteration. Additionally, an analytical solution under steady-state linear flow condition is derived and used to verify numerical simulation results for the steady-state linear flow case. The numerical model is applied to evaluate the transient flow behavior at an injection well for non-Darcy flow according to the Barree and Conway model. Results show that the parameter of characteristic length, $\boldsymbol{\tau}$, is more sensitive than other parameters; while the impact of the minimum permeability plateau is shown only at extremely large flow rates or pressure gradients. The proposed numerical modeling approach is suitable for modeling various types of multi-dimensional non-Darcy flow through porous and fractured heterogeneous reservoirs.

Introduction
Darcy's Law, which is the foundation for fluid flow in porous media studies, was developed by H.P.G. Darcy in 1856 (Darcy, 1856). Through his flow experiments in sand packs, Darcy showed that the potential gradient ($\partial P/\partial L$) could be related to the fluid viscosity (μ) and superficial velocity (v) through a constant, k, which is known universally throughout the petroleum industry as "permeability" (Note that the original work by Darcy was expressed in terms of hydraulic head and hydraulic conductivity). Eq. 1 demonstrates this basic relationship:

$$\frac{\partial P}{\partial L} = \frac{\mu v}{k} \tag{1}$$

In his publication, Darcy discusses the difficulties he had with measurements as higher flow rates due to others placing demand on the flow system of the hospital where he was conducting his experiments. As such, his observations and subsequent development of Darcy's Law were based on low flow rates and the observed constant "Darcy" permeability.

In 1901, Forchheimer observed deviations from the linearity of Darcy's Law at the high flow rates that Darcy had been unable to capture. Forchheimer expanded Darcy's linear form into a quadratic flow equation that is now commonly referred to as Forchheimer's Equation (Eq. 2). Even with this additional quadratic term, Eq. 2 could not adequately describe all of Forchheimer's data; therefore, he eventually added an additional cubic term (Eq. 3) to try and account for these deviations. Other authors have also noted the inability of Forchheimer's equations to describe all data sets (Carman, 1973; Fand et al, 1987; Kececioglu and Jiang, 1994; Montillet, 2004; and Barree and Conway, 2004). The effects of these discrepancies can have a large impact on the assessment of a given porous medium as shown in Figure 1. Figure 1 shows an example of experimental data that deviates from the Forcheimer plot. Figure 1 also shows that β is not a constant with increased flow rate.

$$\frac{\partial P}{\partial L} = \frac{\mu v}{k} + \beta \rho v^2 \quad (2)$$

$$\frac{\partial P}{\partial L} = \frac{\mu v}{k} + \beta \rho v^2 + \gamma \rho v^3 \quad (3)$$

where, β = non-Darcy coefficient, 1/m
ρ = fluid density, kg/m^3

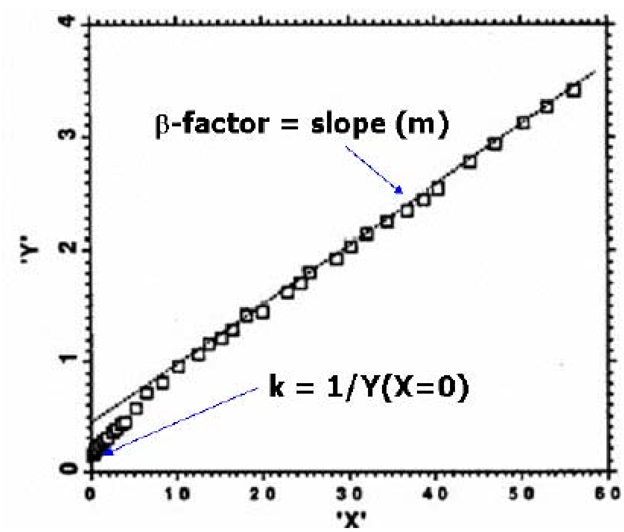

Figure 1. Typical Forcheimer plot where the β-factor is the slope of the line and the permeability (k) is the intercept. Note that the changing slope of the data indicates the β-factor is not a constant in porous media based on the experimental data. (From Martins et al, 1990)

In 2004, Barree and Conway proposed a new general model for non-linear flow in porous media that does not rely on the assumptions of a constant permeability or a constant β. In their model, Darcy's Law is still assumed to apply, but the apparent permeability, treated as a constant in Forchheimer's work, is introduced as a general non-linear function. The Barree and Conway model, Eq. 4, is in the form of a logistic dose (log-dose) equation which is a generic equation that describes a power law slope bounded by two plateau regions. The R_e term in Eq. 4 is defined by Eq. 5.

$$k_{app} = k_{min} + \frac{(k_d - k_{min})}{(1 + R_e^F)^E} \quad (4)$$

$$R_e = \frac{\rho v}{\mu \tau} \quad (5)$$

where, k_{app} = apparent rate-dependent permeability, darcies
k_{min} = minimum permeability at high rate, darcies
k_d = constant Darcy permeability, darcies
R_e = Reynolds number, dimensionless
F, E = exponents, dimensionless
ρ = density, g/cm^3
v = superficial velocity, cm/s
μ = viscosity, cp
τ = characteristic length, 100/cm

The dimensionless form of Eq. 4 can be written as Eq. 6:

$$\eta = \frac{k_{app}}{k_d} = \frac{k_{min}}{k_d} + \frac{1 - \frac{k_{min}}{k_d}}{(1 + N_{Re})^E} \tag{6}$$

There are many benefits with the Barree and Conway equation. First, it provides a single equation to describe the entire range of flow velocities. This is of great benefit in modeling studies, since a single equation can be programmed to model flow without needing to artificially set switchover points from Darcy to non-Darcy flow regimes. Second, since the equation describes the entire range of flow velocities, physical transition zones are also honored and captured as flow velocities increase or decrease. The model also provides for a plateau area at high rates which has been suggested and modeled by other authors (Ergun, 1952; Fang et al, 1987). In summary, the equation developed by Barree and Conway overcomes many of the drawbacks that numerous authors have cited regarding Forchheimer analysis, while still honoring the basics of Darcy and Forchheimer flow behavior.

Laboratory Data and Results

Intensive experiments have been run on proppant packs using a single phase nitrogen non-Darcy flow apparatus (Lopez, 2007). The apparatus uses a cell system consisting of a 20 cm long Tygon tube (to account for embedment) with an inlet diameter of 0.95cm. The cell is filled with proppant and then five pressure ports, spaced 5 cm apart, which are installed along the pack (see Figure 2). The assembled proppant pack is placed in a high pressure vessel that can apply various closure stresses from 0 – 34.5 MPa using a hydraulic oil system. The inlet gas flow rate ranges from 0 – 105 g/sec, which covers most gas production rates encountered in the field.

Proppant samples tested to date include a range of commonly used sizes and types, including ceramics and natural sands, ranging from 12/16 to 100 meshes. Experimental data are analyzed using a regression method for the Forchheimer cubic and quadratic and Barree and Conway techniques (Eqs. 2 – 4). An example of the results using these three techniques is shown in Figure 3. The data plotted in Figure 3 are taken from a ceramic 20/40 proppant under a confining stress of 27.5 MPa. As can be seen in Figure 3, the experimental data agree extremely well with the Barree and Conway model across the entire flow velocity range from low to high gas flow rates. The Forchheimer quadratic correlation overestimates the associated pressure drop, while the Forchheimer cubic correlation underestimates the pressure drop at high gas flow rates. All sample data taken to date show similar agreement with the Barree and Conway equation across the observed flow spectrum.

Figure 4 is a summary plot of all the test data taken to date using the dimensionless form of the Barree and Conway model (Eq. 6). Figure 4 demonstrates that all of the experimental data collapse into one curve as would be expected in a dimensionless form. One plateau of the log-dose equation format is clearly observed at low Reynolds numbers. When converted to field units, the test data shown in Figure 4 cover field gas production rates from less than 707.2 m^3/D to more than 283,168 m^3/D demonstrating that the model is accurate across the intervals of interest for the industry.

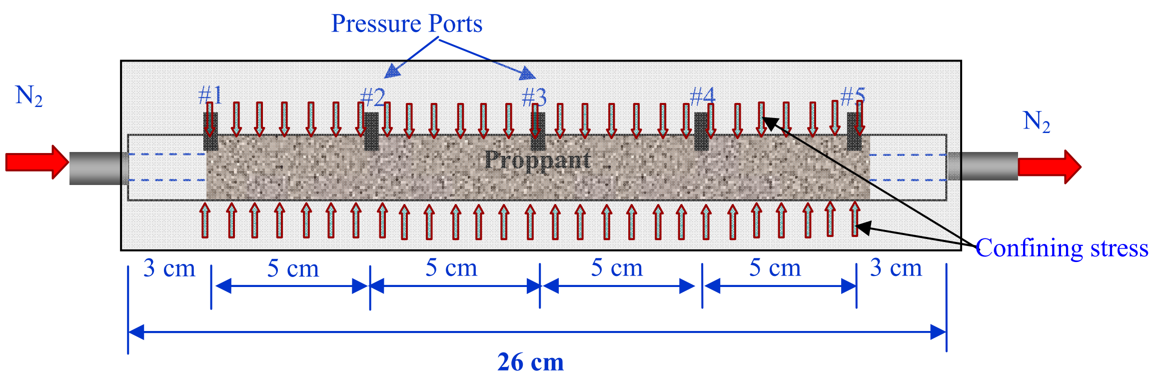

Figure 2. Schematic of the proppant pack used in the non-Darcy flow test system. Proppant is placed in a 20-cm long Tygon tube with an inlet diameter of 0.95cm. Five pressure ports are installed along the pack with a spacing of a 5-cm which provides a pressure profile across the pack, not just at the inlet and outlet. Confining stresses are applied to the pack using hydraulic oil.

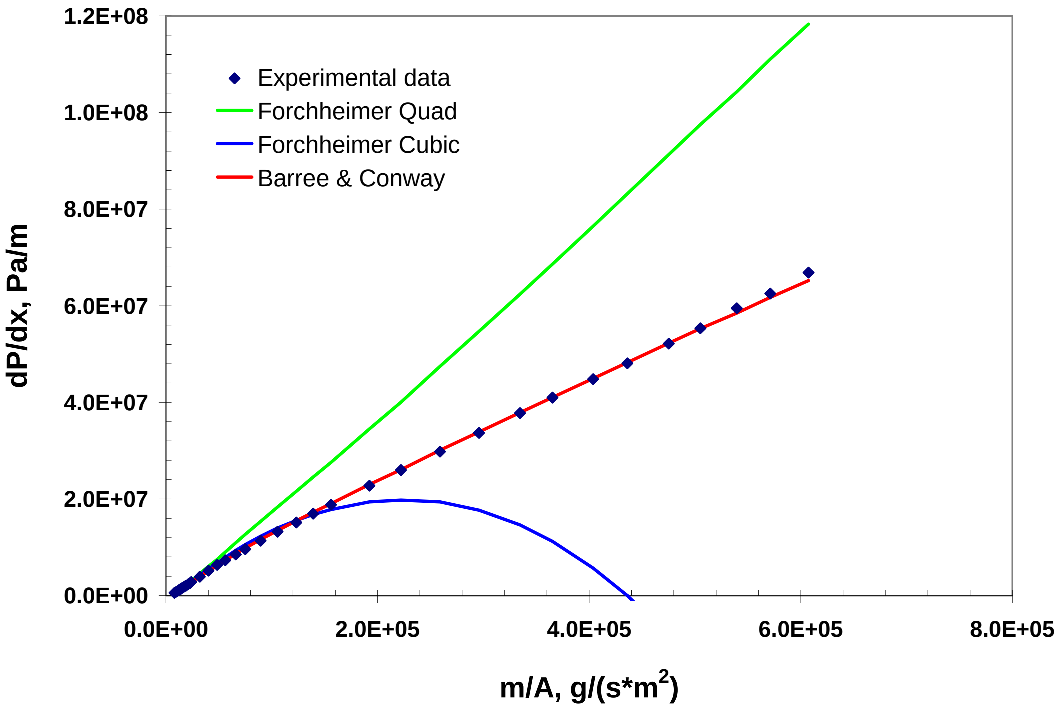

Figure 3. Results of pressure gradient versus mass flow rate for a ceramic 20/40 proppant under a confining stress of 27.5 MPa. The experimental data (blue diamonds) agree with the Barree and Conway model (red) from low to high flow rates. The Forchheimer quadratic correlation (green) overestimates the pressure drop, while the Forchheimer cubic correlation (blue) underestimates the pressure drop at high gas flow rates.

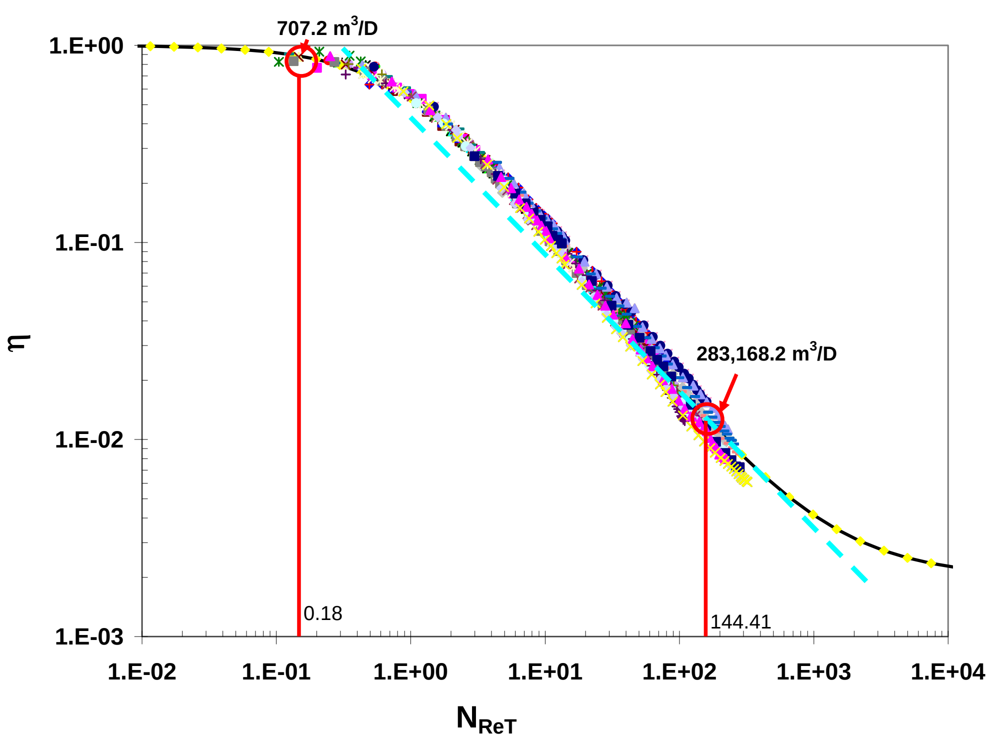

Figure 4. Dimensionless plot of all tested proppants using the Barree and Conway model. As can be seen, all the experimental data collapse onto one curve which matches closely to the theoretical Barree and Conway model (shown as a dashed black and yellow line). One data plateau is clearly observed at low Reynolds numbers and transition zones are captured. The test data covers field production rates from less than 707.2 m^3/D to more than 283,168 m^3/D.

Mathematical Model

In order to compliment the laboratory data results in a reservoir simulation setting, numerical and analytical modeling was performed. In general, consider an isothermal reservoir system consisting of one single-phase fluid (gas or liquid). In an isothermal system containing one fluid, one mass-balance equation is needed to describe the fluid flow in porous media, and mass conservation to the fluid leads to Eq. 7:

$$\frac{\partial}{\partial t}(\phi\rho) = -\nabla \bullet (\rho\mathbf{v}) + q \tag{7}$$

where ϕ is the effective porosity of the medium; ρ is the density of the fluid under reservoir conditions; q is the sink/source term of the phase per unit volume of formation; and **v** is the flow velocity vector (or volumetric flow rate vector), defined in the following Eq. 8, an extended Barree and Conway's model in a vector form for multidimensional flow:

$$-\nabla\Phi = \frac{\mu\mathbf{v}}{k_d\left(k_{mr} + \dfrac{(1-k_{mr})\mu\tau}{\mu\tau + \rho|\mathbf{v}|}\right)} \tag{8}$$

where $\nabla\Phi$ is the flow potential gradient, defined as Eq. 9:

$$\nabla\Phi_\beta = \left(\nabla P_\beta - \rho_\beta g \nabla D\right) \tag{9}$$

where P_β is the pressure of the fluid; g is gravitational acceleration; and D is the depth from a datum.

Numerical Formulation and Solution

The flow equations, shown as Eqs. 7 and 8, for single-phase non-Darcy flow of gas or liquid in porous media as described by the Barree and Conway's model, is highly nonlinear and in general needs to be solved numerically. In this work, the methodology for using a numerical approach to simulate the non-Darcy flow consists of the following three steps: (1) spatial discretization of the mass conservation equation; (2) time discretization; and (3) iterative approaches to solve the resulting nonlinear, discrete algebraic equations. A mass-conserving discretization scheme, based on finite or integral finite-difference or finite-element methods (Pruess et al. 1999) is used and discussed here.

The mass-balance Eq. 7 is discretized in space using a control-volume or integral finite difference concept (Pruess et al. 1999). The control-volume approach provides a general spatial discretization scheme that can represent a one-, two- or three-dimensional domain using a set of discrete meshes. Time discretization is carried out using a backward, first-order, fully implicit finite-difference scheme. Specifically, the non-Darcy flow equations, as discussed above, have been implemented into a three-phase reservoir simulator (Wu, 2000). As implemented numerically, Eq. 7 is discretized in space using an integral finite-difference or control-volume scheme for a porous and/or fractured medium with an unstructured grid. The time discretization is carried out with a backward, first-order, finite-difference scheme. The discrete nonlinear equation for gas or liquid flow at node i is shown in Eq. 10:

$$\left\{(\phi\,\rho)_i^{n+1} - (\phi\,\rho)_i^n\right\}\frac{V_i}{\Delta t} = \sum_{j\in\eta_i} \text{flow}_{ij}^{n+1} + Q_i^{n+1} \tag{10}$$

where the superscript n denotes the previous time level; n+1 is the current time level; V_i is the volume of element i (porous or fractured block); Δt is the time step size; η_i contains the set of neighboring elements (j) (porous or fractured) to which element i is directly connected; flow_{ij}^{n+1} is the mass "flow" term for the fluid between elements i and j; and Q_i is the mass sink/source term at element i, for the fluid.

Based on the 1-D flow rate, Eq. (A.8), with the Barree and Conway model (Appendix A), the mass "flow" term (flow_{ij}^{n+1}) in Eq. 10 for the non-Darcy flow between blocks i and j is evaluated by Eq. 11:

$$\text{flow}_{ij} = \frac{A_{ij}}{2\mu}\left[-(\mu^2\tau - (k_d k_{mr}\rho)_{ij+1/2}\left[\frac{(\Phi_j - \Phi_i)}{d_i + d_j}\right]) + \sqrt{\left(\mu^2\tau - (k_d k_{mr}\rho)_{ij+1/2}\left[\frac{(\Phi_j - \Phi_i)}{d_i + d_j}\right]\right)^2 + 4\mu^2(\rho k_d)_{ij+1/2}\,\tau\left[\frac{(\Phi_j - \Phi_i)}{d_i + d_j}\right]}\,\right] \tag{11}$$

where the subscript ij+1/2 denotes a proper averaging or weighting of properties at the interface between the two elements i and j; A_{ij} is the common interface area between the connected blocks or nodes i and j; d_i is the distance from the center of block i to the common interface of blocks i and j; and the flow potential term in Eq. 11 is defined as Eq. 12:

$$\Phi_i = P_i - \rho_{ij+1/2}\, g\, D_i \qquad (12)$$

Note that in Eq. 10, a discrete equation of mass conservation of the fluid, has the same form regardless of the dimensionality of the model domain, i.e., it applies to one-, two-, or three-dimensional analyses of flow through porous or fractured media (Wu, 2002).

Numerical Solution Scheme: Eq. 10, the discrete, nonlinear equation is solved fully implicitly, using a Newton iteration method. Let us write the discrete nonlinear Eq. 10 in a residual form as Eq. 13:

$$R_i = \left\{ (\phi\,\rho)_i^{n+1} - (\phi\,\rho)_i^{n} \right\} \frac{V_i}{\Delta t} - \sum_{j \in \eta_i} \mathrm{flow}_{ij}^{n+1} - Q_i^{n+1} \qquad (i = 1, 2, 3, \ldots, N) \qquad (13)$$

where N is the total number of nodes/elements/gridblocks of the grid. Eq. 13 defines a set of (N) coupled nonlinear mass balance equations that need to be solved simultaneously. In general, one primary variable per node is needed to use in the Newton iteration for solving one equation per node. We select fluid pressure as the primary variable, and treat all thee rest of the dependent variables, such as viscosity, porosity, and density as secondary variables, which are calculated from the primary variable at each node and at each iteration.

In terms of the primary variable, the residual equation, Eq. 13, at a node i is regarded as a function of the primary variables at not only node i, but also at all its directly neighboring nodes j. The Newton iteration scheme gives rise to Eq. 14:

$$\frac{\partial R_i^{n+1}\left(x_{j,p}\right)}{\partial x_j}\left(\delta x_{i,p+1}\right) = -R_i^{n+1}\left(x_{m,p}\right) \qquad (i = 1, 2, 3, \ldots, N) \qquad (14)$$

where x_j is the primary variable at node i and all its direct neighbors; p is the iteration level; and i =1, 2, 3, …, N. The primary variables in Eq. 14 need to be updated after each iteration shown by Eq. 15:

$$x_{p+1} = x_p + \delta x_{p+1} \qquad (15)$$

The Newton iteration process continues until the residuals, $R_i^{k,n+1}$, or changes in the primary variables, δx_{p+1}, over an iteration are reduced below preset convergence tolerances. In addition, the numerical method is used to construct the Jacobian matrix for Eq. 14, as outlined in Forsyth et al. (1995). At each Newton iteration, Eq. 14, represents a system of N linearized algebraic equations with sparse matrices, which are solved by a linear iterative matrix equation solver.

Treatment of Initial and Boundary Conditions: Dirichlet boundary conditions are handled with the "inactive cell" or "big-volume" method, as normally used in the TOUGH2 code (Pruess et al. 1999). In this method, a constant pressure/saturation node is specified as an inactive cell or with a huge volume, while keeping all the other geometric properties of the mesh unchanged. For flux or Neuman boundary conditions, and multilayered wells, a general procedure for handling such boundary conditions is discussed in Wu et al. (1996 and 2000).

Model Verification and Application

This section presents one verification and one application example to demonstrate the usefulness of the proposed numerical approach in modeling non-Darcy flow in reservoirs. First, we derive steady-state flow analytical solutions and then use them to verify numerical model results. The governing Eq. 7, for one-dimensional linear, horizontal, steady-state flow, is simplified as Eq. 16:

$$\frac{\partial}{\partial x}(\rho v) = 0 \qquad (16)$$

The flow rate according to the Barree and Conway model becomes (Eq. 17 or A.8):

$$v = \frac{-(\mu^2\tau - k_d k_{mr}\rho \frac{\partial P}{\partial L}) + \sqrt{(\mu^2\tau - k_d k_{mr}\rho \frac{\partial P}{\partial L})^2 + 4\mu^2\rho k_d \tau \frac{\partial P}{\partial L}}}{2\mu\rho} \qquad (17)$$

The solution for steady-state incompressible fluid flow is (Eq. 18):

$$P(x) = P_i - \frac{\mu \frac{\dot{m}}{A}(\frac{\dot{m}}{A} + \mu\tau)(L - x)}{(\mu k_d \tau + \frac{\dot{m}}{A} k_d k_{mr})\rho_i} \tag{18}$$

and the solution for steady-state slightly compressible fluid flow is (Eq. 19):

$$P = \frac{1}{c}\left(-(1 - cP_i) \pm \sqrt{(1 - cP_i)^2 + 2c[(1 - \frac{c}{2}P_i)P_i + \frac{\mu \frac{\dot{m}}{A}(\frac{\dot{m}}{A} + \mu\tau)(x - L)}{(\mu k_d \tau + \frac{\dot{m}}{A} k_d k_{mr})\rho_i}]} \right) \tag{19}$$

The detailed development of these two solutions, Eqs. 18 and 19, is provided in Appendix B.

Non-Darcy Flow Behavior: Figure 5 presents several characteristic curves of flow rate versus pressure gradient according to the Barree and Conway model, and shows obvious non-linear flow behavior. The plots in Figure 5 are generated using Eq. 17 for 1-D flow with the test parameters given in Table 1. In examining the non-Darcy flow behavior between the curves of Figure 5, we have found that the parameter, τ, is more sensitive than other parameters for the normal range of pressure gradients. As the value of τ decreases, the flow becomes more non-linear, as shown in Figure 5.

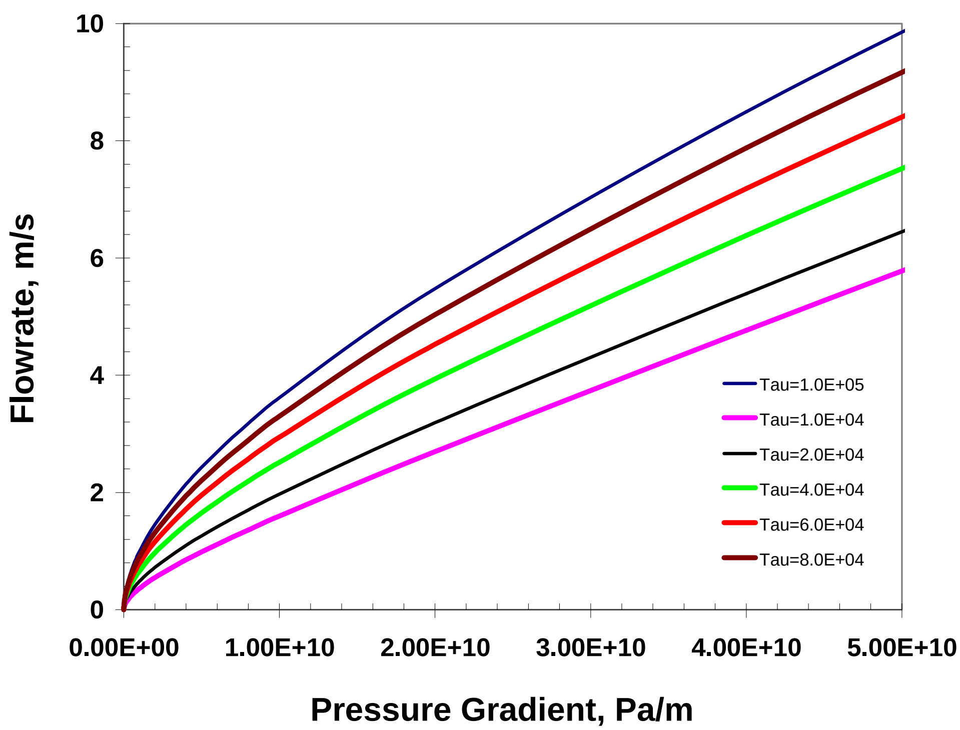

Figure 5. Relationship between flow rate (m/s) and pressure gradient (Pa/m) according to the Barree and Conway model. Relationships for six different τ values are shown. The input parameters used are listed in Table 1.

Model Verification: Here we use the analytical solution, Eq. 18, of 1-D steady-state flow to check the numerical simulation results. In numerical discretization, a 1-D linear reservoir formation 10-m long, with a unit cross-sectional area, is represented by a 1-D uniform linear grid of 1,000 elements with $\Delta x = 0.01$ m. The parameters used for this comparison are listed in Table 2. We compare two cases with different minimum permeability and characteristic length values where Case 1: $k_{min} = 0.1$ Darcy and $\tau = 100{,}000$ (1/m); and Case 2: $k_{min} = 1.0$ Darcy and $\tau = 10{,}000$ (1/m). In the two scenarios, the pressure at the outlet boundary is maintained at 10^7 Pa, and a constant mass production rate is proposed at x = 0 for both the analytical and numerical solutions. The numerical calculation is carried out until steady state is reached. Figure 6 shows the comparison results from the two solutions and indicates that excellent results are obtained from the numerical simulation, as compared to the analytical solution. Figure 6 also shows that for the parameters and their ranges selected in the example cases, the pressure distributions for the two scenarios are nearly linear along the linear flow direction.

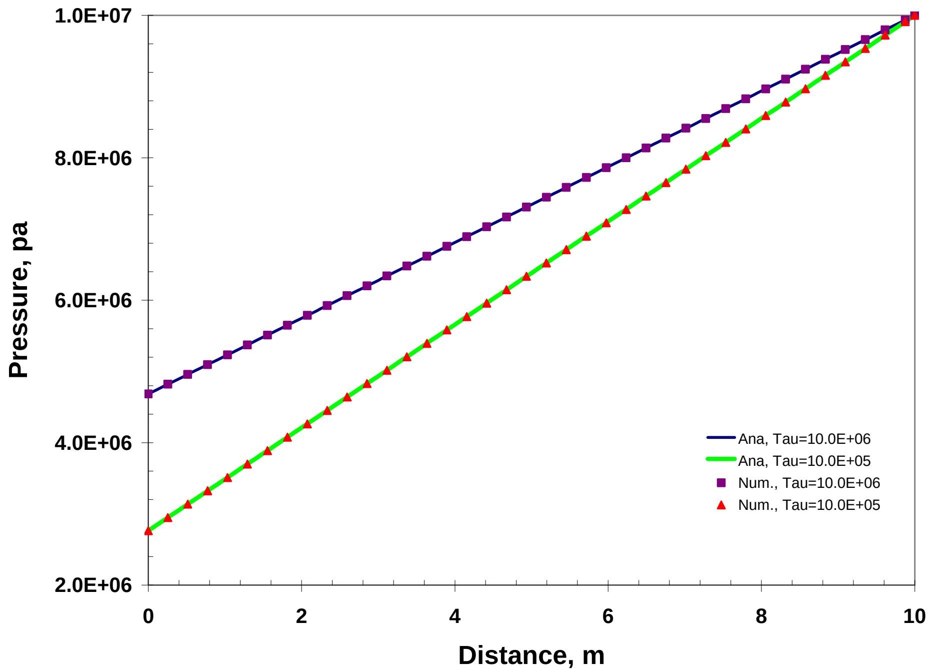

Figure 6. Comparison between the analytical and numerical solutions for 1-D steady-state flow in a linear system. The analytical solution for Case 1 is shown as a solid blue line, while the numerical solution for Case 1 is shown as purple squares. The analytical solution for Case 2 is shown as a solid green line, while the numerical solution for Case 2 is shown as red triangles Model parameters used are listed in Table 2.

Model Application: The application example presents a radial flow problem using the numerical model to calculate transient pressure at an injection well. The reservoir formation is a uniform, radially infinite system (approximated by r_e = 10,000,000 m in the numerical model) of 10 m thick, and is represented by a 1-D radial grid of 1,202 radial increments with a Δr size that increases logarithmically away from the well radius (r_w = 0.1 m). The formation is initially at a constant pressure of 10^7 Pa and is subjected to a constant volumetric injection rate of 1,000 m^3/d at the well, starting at t = 0. Parameters used for the simulation study are listed in Table 3. Figure 7 presents the results of the simulated transient pressure responses at the well and a comparison for the two subject cases with different minimum permeability and characteristic length values of Case 1: k_{min} = 0.1 Darcy and τ = 100,000 (1/m) and Case 2: k_{min} = 1.0 Darcy and τ = 10,000 (1/m). In Figure 7, the lower, dashed curve shows the results for Case 1 and the upper, solid curve shows the results for Case 2. The larger pressure increases in Case 2 indicate that there is more flow resistance for the Case 2 system, as the value of the characteristic length, τ, becomes smaller. It is also interesting to note that in both cases, the later time pressure responses have a linear relationship with time on the semi-log plot, which is similar to Darcy flow behavior.

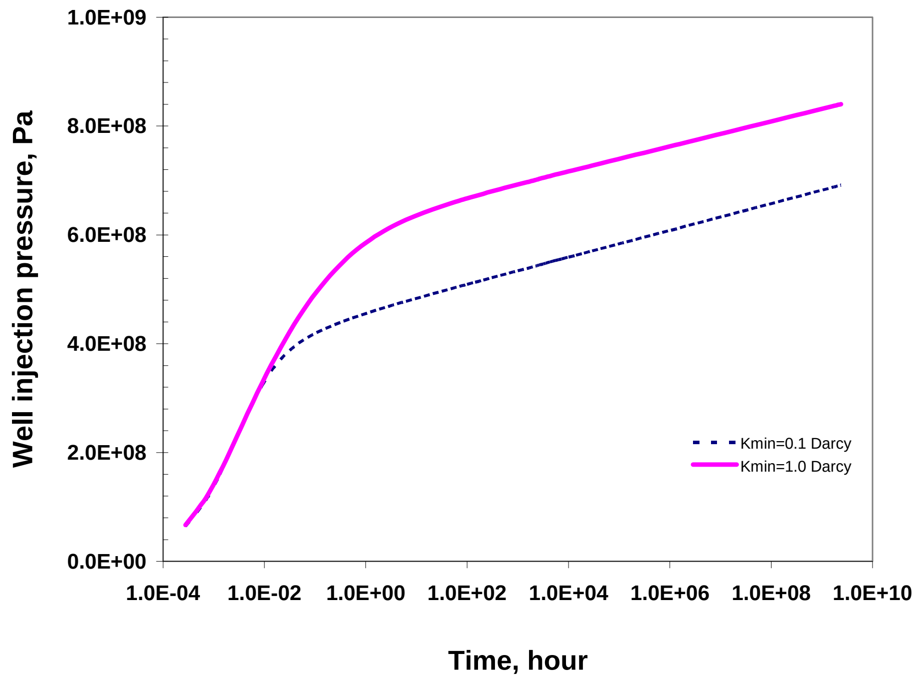

Figure 7. Transient pressure responses simulated at an injection well for 1-D radial flow. The dashed blue line shows the results for Case 1, while the solid magenta line shows the results for Case 2. Higher resistance is demonstrated in the Case 2 system. The simulation parameters used are listed in Table 3.

Conclusions

Laboratory data from proppant pack flow tests that support the Barree and Conway model has been presented. This data set includes a matrix of proppant types and sizes and spans the range of most field gas rates. In an effort to model non-Darcy flow in porous and fractured media and compliment the laboratory data, a mathematical/numerical model is developed by incorporating the Barree and Conway model into a general-purpose reservoir simulator. The mathematical formulation for this inclusion is provided and is based on unstructured grid of control-volume concept and fully implicitly Newton iteration. In addition, several analytical solutions under steady-state linear flow conditions are derived and presented. One of the analytical solutions is then used to verify the numerical simulation results for the steady-state linear flow case.

As an example of application, the numerical model is applied to evaluate the transient flow behavior at an injection well for non-Darcy flow according to the Barree and Conway model. This model results indicate the parameter of characteristic length, τ, is more sensitive than other parameters; while the impact of the minimum permeability plateau is shown only at extremely large flow rates or pressure gradients. The proposed numerical modeling approach is suitable for modeling various types of multi-dimensional non-Darcy flow through porous and fractured heterogeneous reservoirs. The analytical solutions and the numerical simulators from this work can be used for analyzing non-Darcy flow behavior from both laboratory, well flow and field studies.

Acknowledgements

The authors wish to thank the members of the Fracturing, Acidizing, Stimulation Technology (FAST) Consortium located at the Colorado School of Mines and the Stimlab Proppant Consortium for their support. Yu-Shu Wu would also like to thank the support from Sinopec Inc. of China through the National Basic Research Program of China (973 Program).

Nomenclature

A	=	Cross section area of flow, m^2
A_{ij}	=	Common interface area between the connected blocks or nodes i and j
c	=	Compressibility of porous media, 1/Pa
D	=	Depth from a datum
d_i	=	Distance from the center of block i to the common interface of blocks i and j
F,E	=	Exponents, dimensionless

g	=	Gravitational acceleration constant
k_{app}	=	Apparent rate-dependent permeability, darcies
k_{min}	=	Minimum permeability at high rate, darcies
k_{mr}	=	Minimum permeability relative to Darcy permeability, fraction
L	=	Length, m
$\dot{m}$	=	Fluid mass flow rate, gm/sec
M	=	Molecular gas weight
N	=	Total number of nodes/elements/gridblocks of the grid
P_i	=	Initial pressure, Pa
$\partial P/\partial L$	=	Potential gradient, Pa/m
Q	=	Fluid volumetric flow rate, m^3/sec
Q_i	=	Mass sink/source term at element i, for the fluid
R	=	Gas universal constant
R_e	=	Reynolds number, dimensionless
T	=	Temperature, ^oK
Δt	=	Time step size
v	=	Superficial velocity, m/sec
z	=	Gas z factor
β	=	non-Darcy coefficient, 1/m or 1/cm
ρ	=	Fluid density, kg/m^3
ρ_i	=	Initial density, kg/m^3
μ	=	Fluid viscosity, Pois or Pa.s
τ	=	Characteristic length, m/10000
R_e	=	Reynolds number, dimensionless
ϕ	=	Effective porosity of the medium
$\nabla\Phi$	=	Flow potential gradient

References

Barree, R.D. and Conway, M.W. 2004. Beyond Beta Factors: A Complete Model for Darcy, Forchheimer and Trans-Forchheimer Flow in Porous Media. Paper SPE 89325 presented at the 2004 Annual Technical Conference and Exhibition, Houston, Texas 26-29 September.

Carman, P.C. 1937. Fluid Flow Through Granular Beds. *Transactions Institution of Chemical Engineers* **15** (150).

Darcy, H. P. G. 1856. The Public Fountains of the City of Dijon. Bookseller of the Imperial Corps of Bridges, Highways and Mines, Quay of Augustins, **49**; English translation http://biosystems.okstate.edu/darcy/English/Index.html.

Ergun, S. 1952. Fluid Flow Through Packed Columns. *Chemical Engineering Progress* **48** (89).

Fand, R.M., Kim, B.Y.K, Lam, A.C.C. and Phan, R.T. 1987. Resistance to the Flow of Fluids Through Simple and Complex Porous Media Whose Matrices Are Composed of Randomly Packed Spheres. *Transactions of the ASME* **109** (268).

Forchheimer, P.: "Wasserbewegung durch Bode," ZVDI (1901) 45, 1901.

Forsyth, P. A., Y. S. Wu and K. Pruess. 1995. Robust Numerical Methods for Saturated-unsaturated Flow with Dry Initial Conditions in Heterogeneous Media. *Advance in Water Resources* **18**, p. 25-38.

Kececioglu, I. and Jiang, Y. 1994. Flow Through Porous Media of Packed Spheres Saturated with Water. *Transactions of ASME* **116** (164).

Martins, J.P., Milton-Taylor, D. and Leung, H.K. 1990. The Effects of Non-Darcy Flow in Propped Hydraulic Fractures. Paper SPE 20790 presented at the 1990 SPE Annual Technical Conference and Exhibition, New Orleans, Louisiana, 23 – 26 September.

Montillet, A. 2004. Flow Through a Finite Packed Bed of Spheres : A Note on the Limit of Applicability of the Forchheimer Type Equation. *Journal of Fluids Engineering* **126** (139).

Lopez. H. D. 2007. Experimental Analysis and Macroscopic and Pore-level Flow Simulations to Compare Non-Darcy Flow Models in Porous Media. PhD dissertation, Colorado School of Mines, Golden, Colorado.

Pruess, K., C. Oldenburg and G. Moridis. 1999. *TOUGH2 User's Guide, Version 2.0,* Report LBNL-43134, Berkeley, California: Lawrence Berkeley National Laboratory.

Wu, Y. S. 2002. Numerical Simulation of Single-Phase and Multiphase Non-Darcy Flow in Porous and Fractured Reservoirs. *Transport in Porous Media* **49** (2): 209-240.

Wu, Y. S. 2000. A virtual node method for handling wellbore boundary conditions in modeling multiphase flow in porous and fractured media. *Water Resources Research* **36** (3): 807-814.

Wu, Y. S., Forsyth P. A. and Jiang H. 1996. A consistent approach for applying numerical boundary conditions for subsurface flow, *Journal of Contaminant Hydrology* **23**: 157-185.

Table 1. Parameters Used in Figure 5 for Plotting Relationships Between Flow Rate and Pressure Gradient

Parameter	Value	Unit
Darcy permeability	$k_d = 10$	Darcy
Minimum permeability	$k_{min} = 0.1$	Darcy
Viscosity	μ=0.001	Pa·s
Density	ρ =1,000	kg/m^3
Characteristic length	τ=10,000 -100,000	1/m

Table 2. Parameters Used for Model Verification of Checking Numerical Simulation Results Against The Analytical Solution, as Shown in Figure 6

Parameter	Value	Unit
Cross section area	A = 1	m^2
Darcy permeability	$k_d = 10$	Darcy
Minimum permeability	$k_{min} = 0.1, 1.0$	Darcy
Viscosity	μ=0.001	Pa·s
Characteristic length	τ=100,000, 10,000	1/m
Density	ρ =1,000	kg/m^3
Mass production rate	$\dot{m} = 5$	kg/s
Pressure at outer boundary	$P_i = 10^7$	Pa

Table 3. Parameters Used for Simulation Transient Checking Numerical Simulation Results Against the Analytical Solution, as Shown in Figure 6

Parameter	Value	Unit
Darcy permeability	$k_d = 10$	Darcy
Minimum permeability	$k_{min} = 0.1, 1.0$	Darcy
Viscosity	μ=0.001	Pa·s
Reference density	ρ=1,000	kg/m^3
Volumetric Injection rate	q = 1,000	m^3/d
Total compressibility of fluid and rock	$C_T = 6.0\times10^{-10}$	1/Pa
Well radius	$r_w = 0.1$	m
Formation thickness	h = 10	m
Initial formation gas pressure	$P_i = 10^7$	Pa

Appendix A. Relationship of flow rate versus pressure gradient with the Barree and Conway model

The flow rate of 1-D linear flow with the Barree and Conway equation (Barree and Conway, 2004) for fluid velocity is derived and provided in Eqs. A.1 – A.8.

$$\frac{\partial P}{\partial x}=\frac{\mu v}{k_d(k_{mr}+\frac{1-k_{mr}}{1+\frac{\rho v}{\mu\tau}})} \quad (A.1)$$

$$\frac{\partial P}{\partial x}=\frac{\mu v}{k_d(k_{mr}+\frac{k_{mr}\mu\tau+k_{mr}\rho v+\mu\tau-k_{mr}\mu\tau}{\mu\tau+\rho v})} \quad (A.2)$$

$$\frac{\partial P}{\partial x}=\frac{\mu v}{k_d(\frac{k_{mr}\mu\tau+k_{mr}\rho v+\mu\tau-k_{mr}\mu\tau}{\mu\tau+\rho v})} \quad (A.3)$$

$$\frac{\partial P}{\partial x}=\frac{\mu v(\mu\tau+\rho v)}{k_d(k_{mr}\rho v+\mu\tau)} \quad (A.4)$$

$$k_d k_{mr}\rho v\frac{\partial P}{\partial x}+k_d\mu\tau\frac{\partial P}{\partial x}=\mu^2\tau v+\mu\rho v^2 \quad (A.5)$$

$$\mu\rho v^2+(\mu^2\tau-k_d k_{mr}\rho\frac{\partial P}{\partial x})v-k_d\mu\tau\frac{\partial P}{\partial x}=0 \quad (A.6)$$

$$v=\frac{-(\mu^2\tau-k_d k_{mr}\rho\frac{\partial P}{\partial x})\pm\sqrt{(\mu^2\tau-k_d k_{mr}\rho\frac{\partial P}{\partial x})^2+4\mu^2\rho k_d\tau\frac{\partial P}{\partial x}}}{2\mu\rho} \quad (A.7)$$

$$v=\frac{-(\mu^2\tau-k_d k_{mr}\rho\frac{\partial P}{\partial x})+\sqrt{(\mu^2\tau-k_d k_{mr}\rho\frac{\partial P}{\partial x})^2+4\mu^2\rho k_d\tau\frac{\partial P}{\partial x}}}{2\mu\rho} \quad (A.8)$$

Appendix B. Steady-state flow solutions for incompressible and slightly compressible liquids and gas

The solutions for steady-state single phase linear flow of incompressible, slightly compressible, and compressible fluids are provided by Eqs. B.1 – B.29.

Governing equation for steady-state linear flow in porous media:

$$\frac{\partial}{\partial x}(\rho v)=0 \quad (B.1)$$

Integrating Eq. (B.1) leads to

$$\rho v=C \quad (B.2)$$

According to flow velocity and mass flow rate definition, we have

$$v=\frac{Q}{A} \quad (B.3)$$

$$\dot{m} = \rho Q \quad \text{(B.4)}$$

Substituting Eqs. B.3 and B.4 into Eq. B.2

$$\rho v = \rho \frac{Q}{A} = \frac{\dot{m}}{A} \quad \text{(B.5)}$$

Substituting Eq. A.8 into Eq. B.5

$$\rho \frac{-(\mu^2\tau - k_d k_{mr}\rho \frac{\partial P}{\partial x}) + \sqrt{(\mu^2\tau - k_d k_{mr}\rho \frac{\partial P}{\partial x})^2 + 4\mu^2\rho k_d \tau \frac{\partial P}{\partial x}}}{2\mu\rho} = \frac{\dot{m}}{A} \quad \text{(B.6)}$$

Rearranging Eq. B.6

$$-(\mu^2\tau - k_d k_{mr}\rho \frac{\partial P}{\partial x}) + \sqrt{(\mu^2\tau - k_d k_{mr}\rho \frac{\partial P}{\partial x})^2 + 4\mu^2\rho k_d \tau \frac{\partial P}{\partial x}} = 2\mu \frac{\dot{m}}{A} \quad \text{(B.7)}$$

Recasting Eq. B.7

$$\sqrt{(\mu^2\tau - k_d k_{mr}\rho \frac{\partial P}{\partial x})^2 + 4\mu^2\rho k_d \tau \frac{\partial P}{\partial x}} = 2\mu \frac{\dot{m}}{A} + (\mu^2\tau - k_d k_{mr}\rho \frac{\partial P}{\partial x}) \quad \text{(B.8)}$$

Eliminating the square root in Eq. B.8

$$(\mu^2\tau - k_d k_{mr}\rho \frac{\partial P}{\partial x})^2 + 4\mu^2\rho k_d \tau \frac{\partial P}{\partial x} = (2\mu \frac{\dot{m}}{A} + (\mu^2\tau - k_d k_{mr}\rho \frac{\partial P}{\partial x}))^2 \quad \text{(B.9)}$$

Recasting Eq. B.9

$$(\mu^2\tau - k_d k_{mr}\rho \frac{\partial P}{\partial x})^2 + 4\mu^2\rho k_d \tau \frac{\partial P}{\partial x} = (2\mu \frac{\dot{m}}{A})^2 + (\mu^2\tau - k_d k_{mr}\rho \frac{\partial P}{\partial x})^2 + 2 * 2\mu \frac{\dot{m}}{A} * (\mu^2\tau - k_d k_{mr}\rho \frac{\partial P}{\partial x}) \quad \text{(B.10)}$$

Simplifying Eq. B.10

$$4\mu^2\rho k_d \tau \frac{\partial P}{\partial x} = (2\mu \frac{\dot{m}}{A})^2 + 2 * 2\mu \frac{\dot{m}}{A} * (\mu^2\tau - k_d k_{mr}\rho \frac{\partial P}{\partial x}) \quad \text{(B.11)}$$

Simplifying Eq. B.11

$$\mu\rho k_d \tau \frac{\partial P}{\partial x} = \mu (\frac{\dot{m}}{A})^2 + \frac{\dot{m}}{A}\mu^2\tau - \frac{\dot{m}}{A} k_d k_{mr}\rho \frac{\partial P}{\partial x} \quad \text{(B.12)}$$

Rearranging Eq. B.12

$$(\mu k_d \tau + \frac{\dot{m}}{A} k_d k_{mr})\rho \frac{\partial P}{\partial x} = \mu \frac{\dot{m}}{A}(\frac{\dot{m}}{A} + \mu\tau) \quad \text{(B.13)}$$

Integrating Eq. B.13

$$(\mu k_d \tau + \frac{\dot{m}}{A} k_d k_{mr})\int \rho dP = \mu \frac{\dot{m}}{A}(\frac{\dot{m}}{A} + \mu\tau)\int dx \quad \text{(B.14)}$$

For incompressible single-phase ($\rho = \rho_i$) flow:

$$(\mu k_d \tau + \frac{\dot{m}}{A} k_d k_{mr})\rho_i P = \mu \frac{\dot{m}}{A}(\frac{\dot{m}}{A} + \mu\tau)x + C \quad \text{(B.15)}$$

Using Boundary Condition B.16:

$$C=(\mu k_d\tau+\frac{\dot m}{A}k_d k_{mr})\rho_i P_i-\mu\frac{\dot m}{A}(\frac{\dot m}{A}+\mu\tau)L \tag{B.16}$$

Substituting B.16 into B.15:

$$(\mu k_d\tau+\frac{\dot m}{A}k_d k_{mr})\rho_i P=\mu\frac{\dot m}{A}(\frac{\dot m}{A}+\mu\tau)x+(\mu k_d\tau+\frac{\dot m}{A}k_d k_{mr})\rho_i P_i-\mu\frac{\dot m}{A}(\frac{\dot m}{A}+\mu\tau)L$$

or

$$P=P_i-\frac{\mu\frac{\dot m}{A}(\frac{\dot m}{A}+\mu\tau)(L-x)}{(\mu k_d\tau+\frac{\dot m}{A}k_d k_{mr})\rho_i} \tag{B.17}$$

For single phase slightly compressible liquid flow

$$\rho=\rho_i\exp(c(P-P_i)) \tag{B.18}$$

In porous media flow, Eq. B.18 is usually simplified as

$$\rho=\rho_i(1+c(P-P_i)) \tag{B.19}$$

Substituting Eq. B.19 to Eq. B.20

$$(\mu k_d\tau+\frac{\dot m}{A}k_d k_{mr})\int\rho_i(1+c(P-P_i))dP=\mu\frac{\dot m}{A}(\frac{\dot m}{A}+\mu\tau)\int dx \tag{B.20}$$

For liquid phase, the compressibility is usually treated as a constant, integrating Eq. B.14

$$(\mu k_d\tau+\frac{\dot m}{A}k_d k_{mr})\rho_i[(1-cP_i)P+\frac{c}{2}P^2]=\mu\frac{\dot m}{A}(\frac{\dot m}{A}+\mu\tau)x+C \tag{B.21}$$

Boundary condition:

$$x=L,\ \ P=P_i \tag{B.22}$$

Rearranging Eq. B.18,

$$C=(\mu k_d\tau+\frac{\dot m}{A}k_d k_{mr})\rho_i(P_i-\frac{c}{2}P_i^2)-\mu\frac{\dot m}{A}(\frac{\dot m}{A}+\mu\tau)L \tag{B.23}$$

Substitute Eq. B.23 to Eq. B.21,

$$(\mu k_d\tau+\frac{\dot m}{A}k_d k_{mr})\rho_i[\frac{c}{2}P^2+(1-cP_i)P]=\mu\frac{\dot m}{A}(\frac{\dot m}{A}+\mu\tau)(x-L)+(\mu k_d\tau+\frac{\dot m}{A}k_d k_{mr})\rho_i(P_i-\frac{c}{2}P_i^2) \tag{B.24}$$

Dividing Eq. B.24 by $(\mu k_d\tau+\frac{\dot m}{A}k_d k_{mr})\rho_i$, and rearranging

$$\frac{c}{2}P^2+(1-cP_i)P-(1-\frac{c}{2}P_i)P_i-\frac{\mu\frac{\dot m}{A}(\frac{\dot m}{A}+\mu\tau)(x-L)}{(\mu k_d\tau+\frac{\dot m}{A}k_d k_{mr})\rho_i}=0 \tag{B.25}$$

Pressure P can be calculated as below,

$$P=\frac{-(1-cP_i)\pm\sqrt{(1-cP_i)^2+2c[(1-\frac{c}{2}P_i)P_i+\frac{\mu\frac{\dot m}{A}(\frac{\dot m}{A}+\mu\tau)(x-L)}{(\mu k_d\tau+\frac{\dot m}{A}k_d k_{mr})\rho_i}]}}{c} \tag{B.26}$$

The pressure P in any point of L is the positive root of Eq. B.24.

For single phase gas flow, the density is described by the real gas law

$$\rho = \frac{PM}{zRT} \tag{B.27}$$

$$(\mu k_d \tau + \frac{\dot{m}}{A} k_d k_{mr}) \int_{P_i}^{P} \frac{PM}{zRT} dP = \mu \frac{\dot{m}}{A} (\frac{\dot{m}}{A} + \mu \tau) \int_{0}^{x} dx \tag{B.28}$$

Then the steady-state flow solution to single phase gas is given by,

$$(\mu k_d \tau + \frac{\dot{m}}{A} k_d k_{mr}) \frac{M}{RT} \int_{P_i}^{P} \frac{P}{z} dP = \mu \frac{\dot{m}}{A} (\frac{\dot{m}}{A} + \mu \tau) x \tag{B.29}$$